IET Microwaves, Antennas & Propagation

Research Article

IET Journals
The Institution of Engineering and Technology

Novel coated differentially fed dual-band fractal antenna for implantable medical devices

ISSN 1751-8725
Received on 13th December 2018
Revised 22nd September 2019
Accepted on 23rd October 2019
E-First on 11th November 2019
doi: 10.1049/iet-map.2018.6171
www.ietdl.org

Yi Fan[1,2], Hui Liu[1], XiongYing Liu[1,3] ✉, Yan Cao[3], ZhongXin Li[1], Manos M. Tentzeris[4]

[1]*School of Electronic and Information Engineering, South China University of Technology, Guangzhou, People's Republic of China*
[2]*School of Electronics and Information, Guangdong Polytechnic Normal University, Guangzhou, People's Republic of China*
[3]*National Engineering Technology Research Center for Mobile Ultrasonic Detection, Guangzhou, People's Republic of China*
[4]*School of Electrical and Computer Engineering, Georgia Institute of Technology, Atlanta, USA*
✉ *E-mail: liuxy@scut.edu.cn*

Abstract: A novel differentially fed fractal antenna coated with a layer of a dielectric film and operating at two bands of Medical Implant Communication Services 402–405 MHz and Industrial, Scientific, and Medical 2.4–2.48 GHz, is investigated to enable sufficient data transmission rates, while featuring a 'mode-control' signal to prolong the battery life. The symmetrical fractal technology of Hilbert curve is employed to miniaturise the dimension. To facilitate interfacing with peripheral integrated circuits, differentially feeding is adopted. To demonstrate how common-mode noises are suppressed, for the first time, a detailed analysis about the noise suppression of the differential configuration with two feedings is presented. A layer of thin film is coated around the proposed antenna to isolate the effect of human tissues and alleviate the electromagnetic coupling with human body. Moreover, to draw a design methodological guideline, the key geometrical parameters are analysed numerically and theoretically. Health safety considerations, radiation performance, and link budgets are also discussed to validate the proposed antenna's applicability in biomedical telemetry.

1 Introduction

Owing to their inherent capabilities to detect the human vital signs more accurately and conveniently than the sensors outside the body, the implantable medical devices (IMDs) are getting increasingly popular in the fields of diagnostics, biomonitoring, and therapeutics. Some typical applications include implantable pacemakers, cochlear implants, implantable drug pumps, vagus nerve stimulators and so on [1]. IMDs need to exchange data with the outside base stations/gateways wirelessly. Traditionally, inductive coils have been implemented to undertake this task [2, 3], while they suffer from numerous limitations, such as a low data transmission rate and a limited communication range [4]. There is a growing trend to employ implantable antennas due to their advantages compared to the inductive coils [4–8].

To make the implantable antenna suitable for working in the human body, several issues must be considered. Firstly, in view of the stringent space limitations inside the human body, the implantable antennas should have a compact size. In [9–14], numerous miniaturising technologies, such as using high-permittivity substrates, meandering patches, adding shorting pins, and employing stacked structures, have been listed. Whereas, these kinds of complex configurations increase the overall dimension and the difficulty of antenna fabrication. Due to the self-similarity and space-filling properties, the structure of fractal geometry can lengthen the effective current path, minimising the dimensions of the antenna. Various fractal antennas, such as Minkowski fractal antenna [15], Koch modified microstrip antenna [16], and Fern-fractal-shaped microstrip antenna [17], have been proposed. However, these fractal geometries are too complex, and difficult to be fabricated. Based on the fact that the dissipation of electromagnetic (EM) waves through human tissues is increased with frequency, the implantable antenna should operate at relative lower frequency bands. Hence, the band of 402–405 MHz (i.e. Medical Implant Communication Services (MICS) band), which has been authorised as the implantable antenna's operating frequency by Federal Communications Commission, is commonly used for biomedical data transmission [18–21]. Finally, for the sake of prolonging the battery life of IMDs, the implantable antenna should be low power loss. On the one hand, some single-band implantable antennas have been presented in the literature [13, 22], but considerable energy will be consumed due to uninterruptedly operating of these antennas, hence dual-band implantable antennas will be beneficial to saving energy for the purpose of allowing the IMDs to operate in either a 'sleep' or an 'awake' mode corresponding to different bands [23]. On the other hand, single-fed configurations employed in previously proposed implantable antennas [6–14, 21, 24, 25], require additional matching circuits or baluns, thus increasing the volume and power dissipation of IMDs, complicating their implantation into the human body. Therefore, a differentially fed structure is preferable for the implantable antenna as it allows for an easy direct connection with radio frequency integrated circuits (ICs) [4] and has enhanced common-mode noise suppression. However, to the authors' knowledge, until now there has been no quantitative evaluation of the noise suppression characteristics of previously reported implantable antennas.

In this paper, a coated differentially fed dual-band fractal implantable antenna operating at MICS and Industrial, Scientific, and Medical (ISM) bands is proposed. Instead of employing shorting pins or stacked topologies, the Hilbert curve, a type of space-filling configurations with their inherent self-similarity property, is adopted to effectively increase the electrical length of the current flow, thus miniaturising the dimensions of the proposed antenna and making fabrication easier. Different from [26–28], the proposed antenna, is composed of two pieces of the Hilbert curve with different widths, resonating at the lower and upper bands for the telemedicine. Moreover, differential feeding is adopted. The differentially fed configuration virtually eliminates the loss caused by matching circuits and baluns, and its symmetrical structure enhances the ability of common-signal ('noise') suppression, the first quantitative evaluation of which is studied in this work. The dual-band operation allows IMDs, compatible with commonly used transceivers, such as Zarlink ZL70102 [29], to operate in two modes, thus saving energy and extending the battery life of IMDs. Finally, to alleviate the effect of surrounding lossy muscles, a layer of the biocompatible film has been coated around the fabricated antenna.

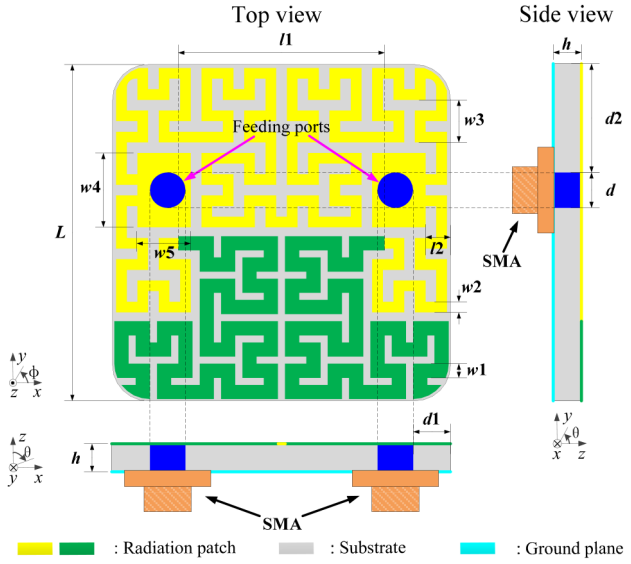

Fig. 1 *Configuration of the proposed antenna geometry*

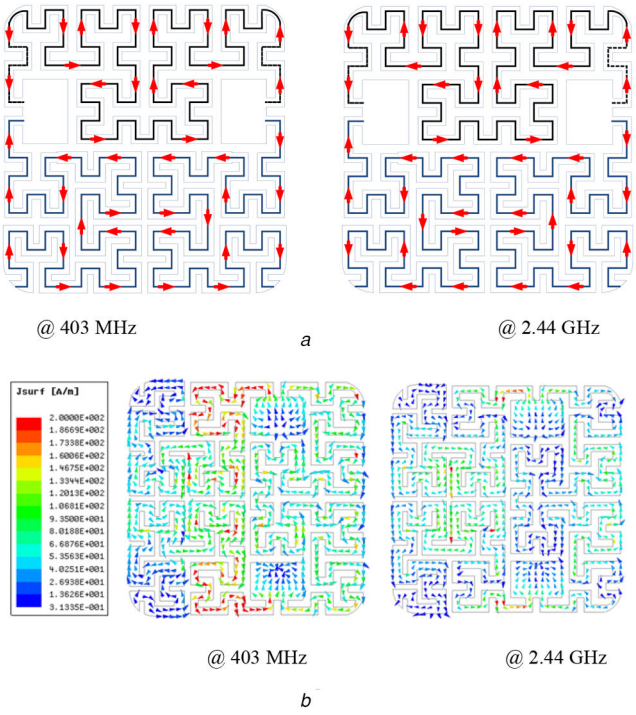

Fig. 2 *Electrical current plots of the proposed antenna at MICS (403 MHz) and ISM (2.44 GHz) bands*

(a) Schematic drawing of current flow, ***(b)*** Simulated electric current distribution

Table 1 Dimensions of the proposed antenna parameters

Parameter	Value, mm	Parameter	Value, mm
L	9.5	*w*1	0.4
*w*2	0.3	*w*3	1.2
*w*4	2.1	*w*5	1.5
h	0.635	*d*	1
*d*1	1.1	*d*2	3.1
*l*1	5.8	*l*2	0.7

This paper is organised as follows. In Section 2, the differentially fed antenna and the simulations' setup for practical 'implantable configurations' are introduced. The simulation results and the key design parameters of the proposed antenna are discussed in Section 3. The coating process and the ex-vitro experimental verification results are presented in Section 4. The communication link budgets are analysed in Section 5, followed by the conclusions in Section 6.

2 Antenna design

2.1 Antenna configuration

Fig. 1 displays the structure of the proposed antenna, which is symmetric about the *yz*-plane. One proof-of-concept prototype is etched on the substrate of Rogers RO3210 ($\varepsilon_r = 10.2$; $\tan\delta = 0.003$) with a thickness of h, has a square shape with the side width of L, and the four corners of the substrate are polished into one-fourth convex arcs with the radius of 1 mm. The rounded square shape can eliminate the effect of sharp antenna's angles that could potentially hurt in-body tissues in proximity. The radiation patch has the shape of the Hilbert curve, which is a continuous fractal space-filling curve. The width of Hilbert curve is non-uniform, wherein the line on one side labelled with green colour in Fig. 1 has the width of $w1$, while the Hilbert curve in yellow has different width of $w2$. As shown in Fig. 2, due to the self-similarity property of Hilbert curve, the current-flow path can be easily extended in terms of electrical length within the same antenna's surface area. Specifically, the current path lengths from the feeding to the near-open-circuit endpoints are approximately equal to a quarter wavelength and six-fourth wavelengths at MICS and ISM bands, respectively, drastically shrinking the physical dimensions of the proposed antenna. Two copper solid cylinders with the diameter of d are used as the differential-feeding ports. During the experimental verification, the two feeding ports were connected to the inner conductors of 50-Ω coaxial cables, respectively. The bottom side of the substrate is covered by the ground plane. The optimal dimensions of the final prototype design derived with the aid of ANSYS HFSS v.13 are listed in Table 1.

2.2 Definitions of performance-evaluation parameters

Although it is well known that differentially fed antennas feature the merit of noise suppression, so far there have been no previous publications to provide quantitative analysis. To provide design criteria for the evaluation of the performance of noise suppression and even provide benchmarking criteria for future related efforts, some fundamental parameters are defined firstly. As the proposed differential antenna can be equivalent to a two-port network, according to the definition in the literature of [30], the differential-mode and common-mode EM wave's power can be described as

$$\begin{bmatrix} a_{\text{dif}} \\ a_{\text{com}} \end{bmatrix} = \frac{1}{\sqrt{2}} \begin{bmatrix} 1 & -1 \\ 1 & 1 \end{bmatrix} \begin{bmatrix} a_1 \\ a_2 \end{bmatrix}, \tag{1}$$

$$\begin{bmatrix} b_{\text{dif}} \\ b_{\text{com}} \end{bmatrix} = \frac{1}{\sqrt{2}} \begin{bmatrix} 1 & -1 \\ 1 & 1 \end{bmatrix} \begin{bmatrix} b_1 \\ b_2 \end{bmatrix}, \tag{2}$$

where a_i and b_i ($i = 1$ or 2) represent the incident and reflected EM power, respectively. Then the differential reflection coefficient (DRC) Γ_{dif} can be expressed as

$$\begin{aligned} \Gamma_{\text{dif}} &= \left.\frac{b_{\text{dif}}}{a_{\text{dif}}}\right|_{a_{\text{com}}=0} = \left.\frac{b_1 - b_2}{a_1 - a_2}\right|_{a_{\text{com}}=0} \\ &= \frac{1}{2}(S_{11} - S_{12} - S_{21} + S_{22}). \end{aligned} \tag{3}$$

Similarly, the common-mode reflection coefficient Γ_{com} can be defined as

$$\begin{aligned} \Gamma_{\text{com}} &= \left.\frac{b_{\text{com}}}{a_{\text{com}}}\right|_{a_{\text{dif}}=0} = \left.\frac{b_1 + b_2}{a_1 + a_2}\right|_{a_{\text{dif}}=0} \\ &= \frac{1}{2}(S_{11} + S_{12} + S_{21} + S_{22}). \end{aligned} \tag{4}$$

Following the fundamentals of antenna theory, the radiation intensity U is given by the following equation:

$$U = \left(1 - |\Gamma|^2\right) G(\theta, \varphi) \frac{P_{\text{in}}}{4\pi}, \tag{5}$$

where Γ is the reflection coefficient, G is the radiation gain of the antenna by using an isotropic antenna as a reference, P_{in} is the input power, θ and φ are zenith and azimuth angles in spherical coordinates, respectively. Hence, the differential-mode radiation intensity U_{dif} and the common-mode radiation intensity U_{com} are deduced as

$$U_{\text{dif}} = \left(1 - |\Gamma_{\text{dif}}|^2\right) G_{\text{dif}}(\theta, \varphi) \frac{P_{\text{in}}}{4\pi}, \tag{6}$$

$$U_{\text{com}} = \left(1 - |\Gamma_{\text{com}}|^2\right) G_{\text{com}}(\theta, \varphi) \frac{P_{\text{in}}}{4\pi}. \tag{7}$$

Noise is always considered as a common-mode signal in differential structures. To estimate how much noise is suppressed in differentially fed antenna configurations, the common-mode rejection ratio (CMRR) K_{CMR} can be written as

$$K_{\text{CMR}}(\theta, \varphi) = \frac{1 - |\Gamma_{\text{dif}}|^2}{1 - |\Gamma_{\text{com}}|^2} \frac{G_{\text{dif}}(\theta, \varphi)}{G_{\text{com}}(\theta, \varphi)}, \tag{8}$$

similarly to CMRR of differential amplifiers in conventional lumped-element analogue circuits.

2.3 Setup of simulation

To enhance the design efficiency and accuracy in realistic implanted configurations, as shown in Fig. 3, the proposed antenna is firstly simulated by implanting it into a three-layer 'human body' model at a depth of $dp1$ from the muscle surface with the cylindrical layer dimensions approximating those of the human body as shown in Table 2. Due to the fact that the dielectric properties of tissues are dispersive, as listed in Table 3, the permittivity and conductivity of every tissue are given at the centre frequencies of 403 MHz and 2.44 GHz, respectively [31]. Furthermore, to reduce the unwanted EM coupling to nearby tissues and prevent the rejection of the implant, the proposed antenna is surrounded by a 70-μm-thick biocompatible material of alumina with the high relative dielectric constant of $\varepsilon_r = 9.2$ and the low loss tangent of $\tan \delta = 0.008$, thus decreasing the mismatch between the insulated antenna and the ambient tissues.

After preliminary simulations and optimisation with an HFSS approximate three-layer 'human body', the radiation characteristics of the proposed antenna are further verified in the more realistic CST heterogeneous male Zubal phantom, which is closer to the actual conditions. In the Zubal phantom, that is shared by Yale University [32, 33], the dielectric parameters of each tissue at the frequencies of 403 MHz and 2.44 GHz are set according to Cole-Cole formulation [31]. For proof-of-concept demonstration purposes, as displayed in Fig. 4, the proposed antenna is implanted into the muscle layer of the left arm at a depth of $dp2 = 10$ mm.

3 Simulation results and discussion

3.1 Simulated results and operating principle

The values of the simulated DRCs Γ_{dif} for the proposed implanted antenna using the HFSS cylindrical multilayer model and the CST human model are shown in Fig. 5, featuring similar trends with minor discrepancies in both MICS and 2.44-GHz ISM bands.

To evaluate the superior noise suppression capability of the proposed antenna, the values of K_{CMR} are calculated and compared to previously published reference antennas in HFSS simulation environment. Without loss of generality, arranging the coordinate system such that the angle $(\theta, \varphi) = (0, 0)$ is the main direction of communication, only K_{CMR} (0, 0) at MICS and ISM bands is considered. With reference to Fig. 6, the K_{CMR} of the proposed antenna is more than 21.24 and 2.06 dB in the MICS and ISM bands, respectively, significantly better than the prior art reported

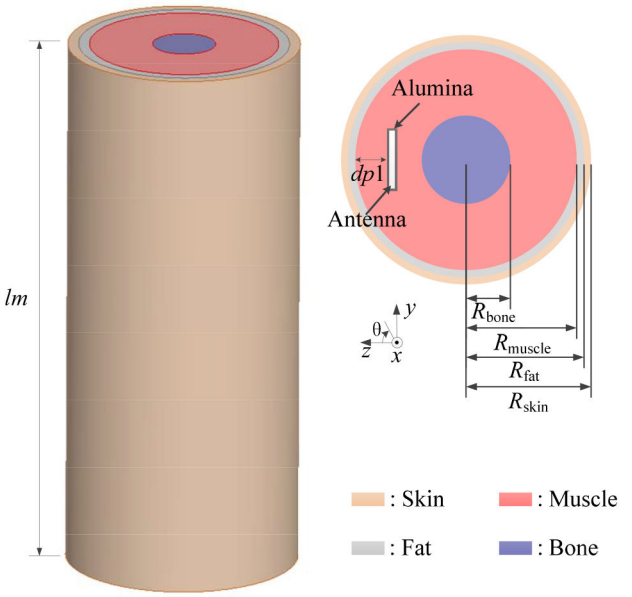

Fig. 3 *'Human body' simulation environment in HFSS*

Table 2 Parameters of HFSS 'human body' simulation setup

Parameter	Value, mm	Parameter	Value, mm
$dp1$	10	lm	200
R_{bone}	12	R_{muscle}	35
R_{fat}	39	R_{skin}	43

Table 3 Dielectric parameters of human tissues

Human tissues	403 MHz		2.44 GHz	
	ε_r	σ, S/m	ε_r	σ, S/m
skin	46.7	0.69	38.0	1.46
fat	11.6	0.08	10.8	0.27
muscle	57.1	0.79	52.7	1.73
bone	22.4	0.24	18.6	0.80

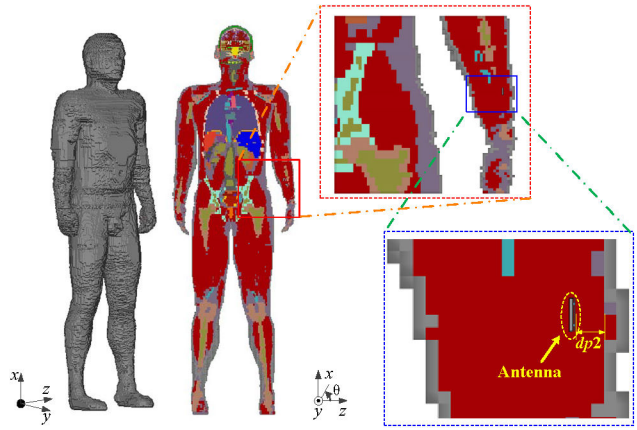

Fig. 4 *Zubal phantom simulation environment in CST*

in [34]. To understand how the proposed antenna works, the EM fields on the xz-plane crossing the antenna's structural centre are analysed. As illustrated in Fig. 7*a*, an electric wall can be placed along the yz-symmetry plane and is equivalent to a shorting plate, when the two feeding ports are fed by differential-mode signals. Hence, as depicted in Fig. 7*b*, the proposed antenna is equivalent to a parallel combination of two planar inverted-F antennas (PIFAs), sharing a common shorting plate. Due to the symmetry of the proposed structure, the operation mechanism is similar to traditional analogue signal differential amplifiers, as displayed in

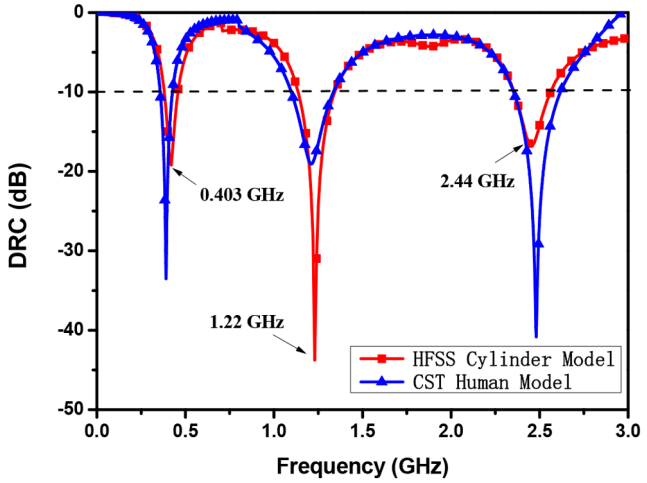

Fig. 5 *DRCs* (Γ_{dif}) *values in HFSS and CST simulators*

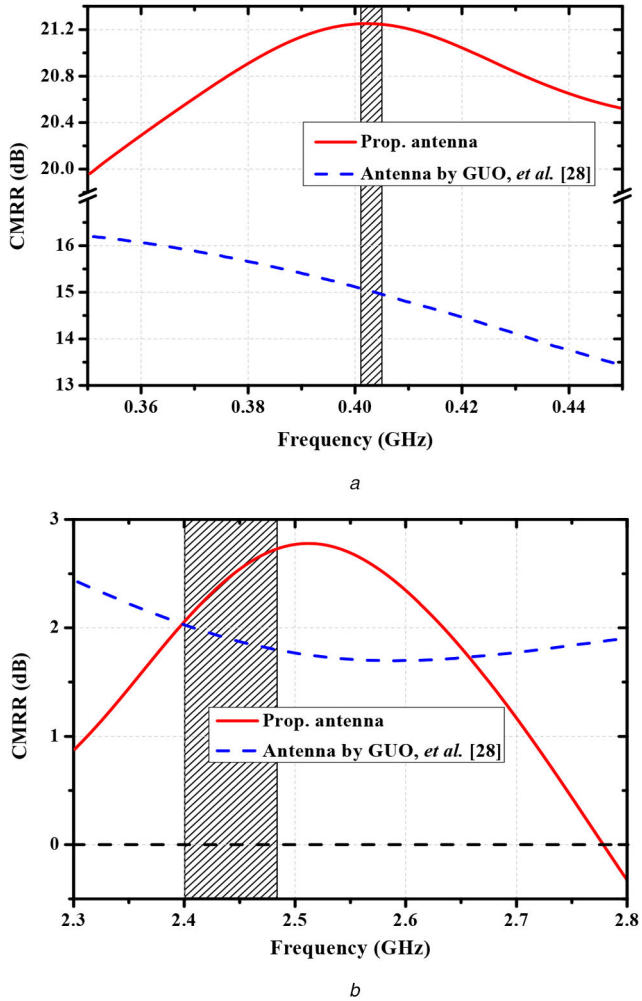

Fig. 6 *KCMR (0, 0) of the proposed antenna*
(a) At MICS band, ***(b)*** At ISM band

Fig. 7*c*. Due to the existence of the electrical wall, as illustrated in Fig. 8, although two ports are very close, the isolation is very high with $|S_{21}|$ less than −15 dB in the bands of 402–405 MHz and 2.4–2.48 GHz. On the other side, when common-mode signals are used to excite the antenna structure, the magnetic field is normal to the *yz*-symmetry plane, as plotted in Fig. 9*a*, effectively placing a magnetic wall (open circuit) in the middle of the Hilbert curves. Following the theory of transmission lines, the input reactance of the open-circuit section, whose length is shorter than a quarter wavelength, is negative being effectively equivalent to capacitors. Thus, equivalent capacitances C_{eq} can be introduced in Fig. 9*b* to

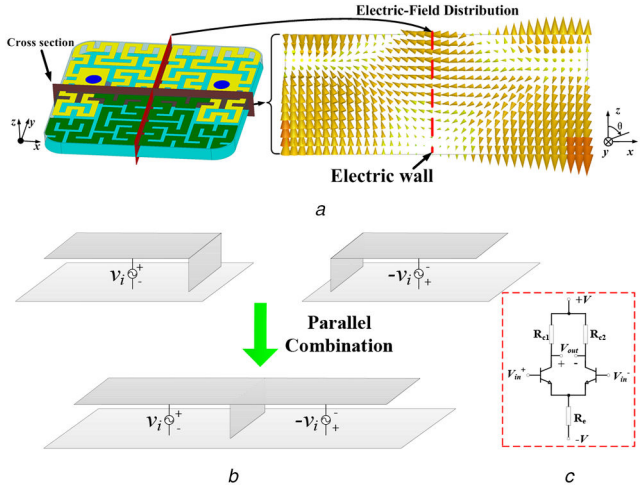

Fig. 7 *Equivalent modelling of the proposed antenna with differential-mode signals*
(a) *Electric field distribution on the cross-section of the proposed antenna using differential feeding,* ***(b)*** *Parallel connected configuration of two PIFAs, and* ***(c)*** *Diagram of differential amplifier circuit*

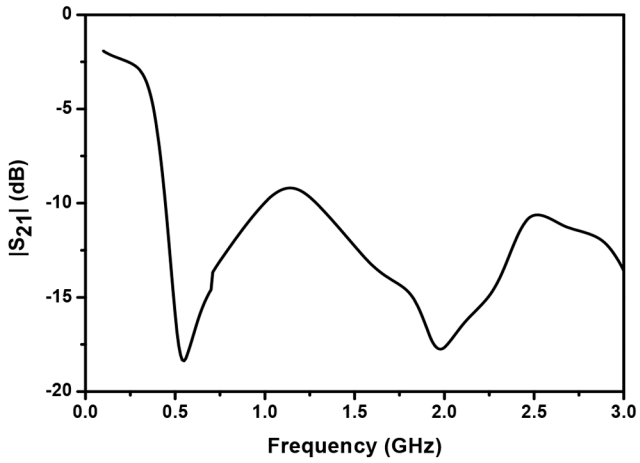

Fig. 8 *S_{21} varies with frequency*

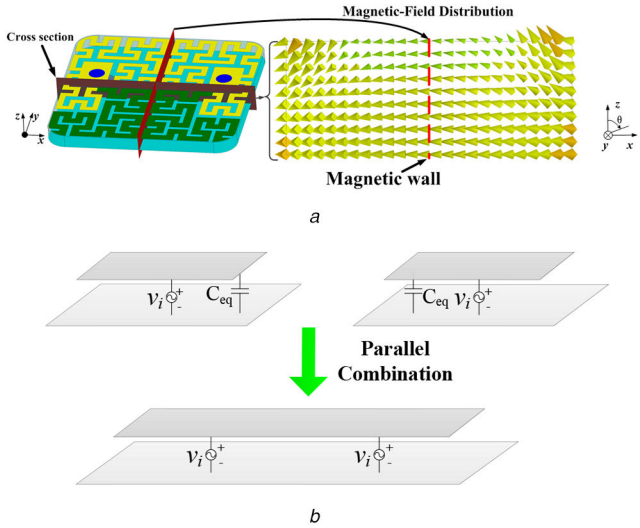

Fig. 9 *Equivalent modelling of the proposed antenna fed by common-mode signals*
(a) Magnetic field distribution on the cross-section of the proposed antenna using common-mode feeding, ***(b)*** Parallel connected configuration of two capacitive patches

represent the electrically short conductive lines that are terminated to the middle plane, i.e. to the equivalent magnetic wall. Through the comparison of the normalised input impedance values shown in

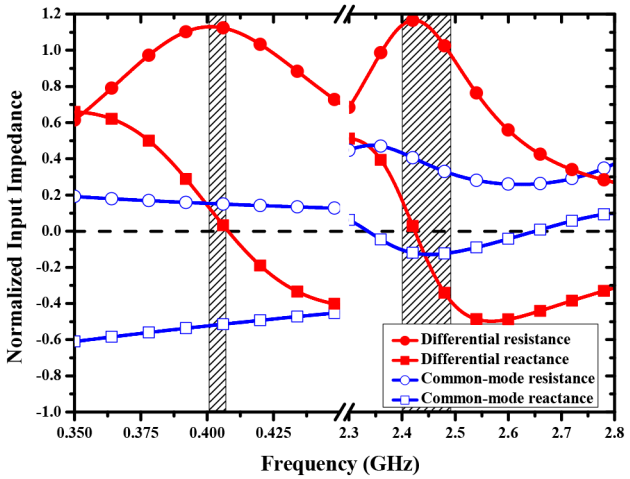

Fig. 10 *Normalised input impedances of differential- and common-modes*

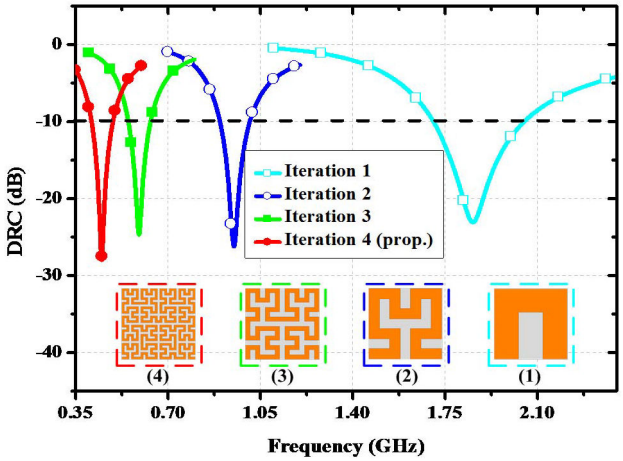

Fig. 11 *Simulated DRCs* (Γ_{dif}) *with different iterations of Hilbert curve*

Fig. 10, it can be clearly observed that the proposed antenna is much easier to match (closer to the normalised value of 1) to a 50-Ω coaxial cable under the differential feeding condition than under the common-mode feeding. According to (8), K_{CMR} is enhanced as Γ_{dif} is decreased and Γ_{com} is increased, thus leading to a stronger common-signal suppression capability.

3.2 Analysis of key parameters

To investigate how the performance of the proposed antenna is influenced and to provide design guidelines, numerous parameters of interest are analysed. With reference to Fig. 11, as the dimension of Hilbert curve, increases on a fixed surface area, the resonant frequency of antenna shifts down, i.e. the antenna size can be miniaturised through increasing the number of iterations of Hilbert curve. Considering actual manufacturing technologies, the width of the Hilbert-curve patch cannot be infinitesimally narrow. Finally, an optimal tradeoff between the convenience of fabrication and the miniaturisation is reached after four iterations.

As illustrated in Fig. 12, the feeding positions also play an important role in the performance enhancement of PIFAs, due to their effects on impedance matching during the differential feeding. Considering an easy fabrication as well as a high performance, the No.4 feeding position was chosen. The changes of input impedance corresponding to different joints (interconnecting geometries of the two antenna sections (yellow and green)) between the two stubs of the PIFA patches are plotted on the Smith chart as shown in Fig. 13. It can be inferred that the relative position of the 'joints' has a significant effect on the reflection coefficient at ISM band, whereas the MICS band remains insensitive to the 'joints' positions.

Some other critical geometrical parameters, such as the widths $w1$ and $w2$ of the two antenna sections (yellow and green), are

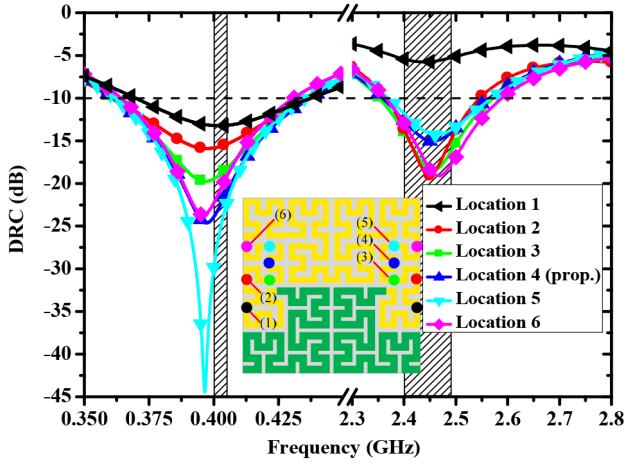

Fig. 12 *Simulated DRCs* (Γ_{dif}) *of the proposed antenna with different feeding ports*

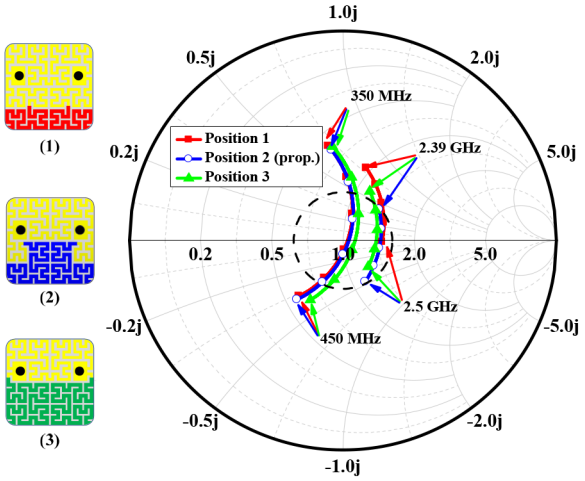

Fig. 13 *Input impedance variation on a Smith chart at MICS and ISM bands with respect to different 'joint' positions*

analysed. With reference to Fig. 14, the resonant frequency shifts to higher bands as $w1$ decreases and $w2$ increases, or vice versa. This is mainly due to the fact that the resonant frequency is approximately equal to $1/2\pi\sqrt{LC}$, wherein the capacitance is proportional to the width of $w1$, and the inductance is inversely proportional to the width of $w2$.

Owing to the large difference of the relative permittivity between the coating alumina film and the human tissue (e.g. muscle), there is a large discontinuity when EM waves propagate outwards, resulting in the majority of the EM energy getting reflected back. Hence, it is essential to analyse the influence of the thickness of the alumina film on the performance of the proposed antenna. Fig. 15 shows the DRC curves, varying with the thickness hc of the alumina film from 50 to 90 μm with a step of 20 μm. As can be seen from the figure, the DRC curves shift to higher frequencies with hc increasing; this is because the thicker the encapsulating alumina film is, the smaller the effective permittivity of the 'near-field' antenna surrounding area consisting of the alumina and the muscle is, hence, smoothing the discontinuity between antenna and surrounding tissues and enhancing EM wave transmission.

3.3 EM radiation properties and safety considerations

As shown in Figs. 16 and 17, the proposed implanted antenna features the strongest radiation in the off-body direction, hence, effectively realising wireless communications between medical devices inside the body and base stations/gateways outside the body. As shown in Fig. 18, the gain in MICS band is almost constant with a maximum value of −28.1 dBi, while the gain at ISM band is lower with a peak gain of −31.3 dBi. There is a

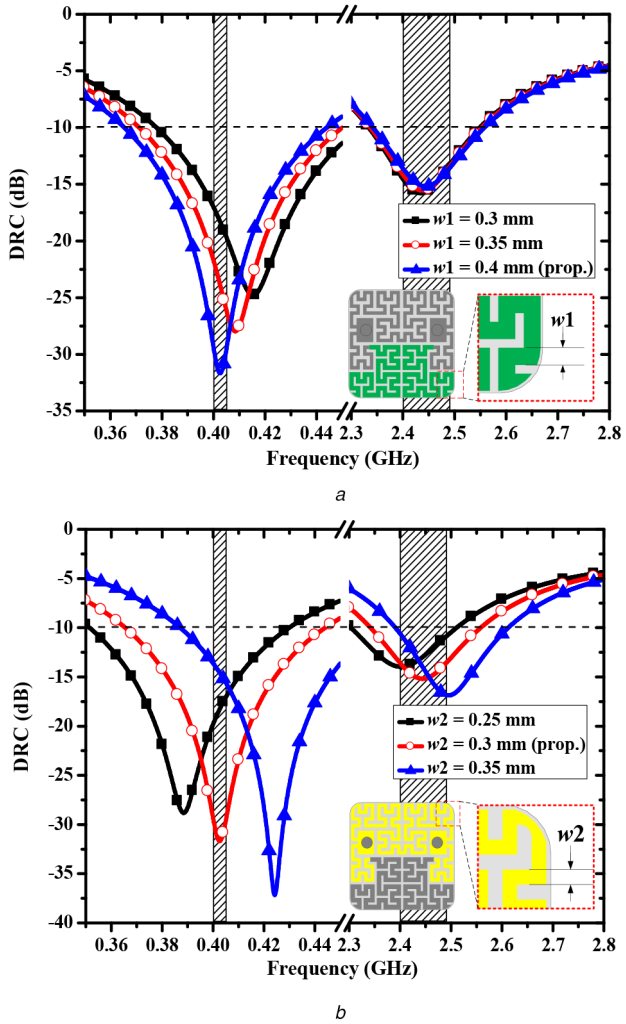

Fig. 14 *Variation of simulated DRCs* (Γ_{dif}) *versus* ***(a)*** $w1$, when $w2 = 0.3$ mm, ***(b)*** $w2$, when $w1 = 0.4$ mm

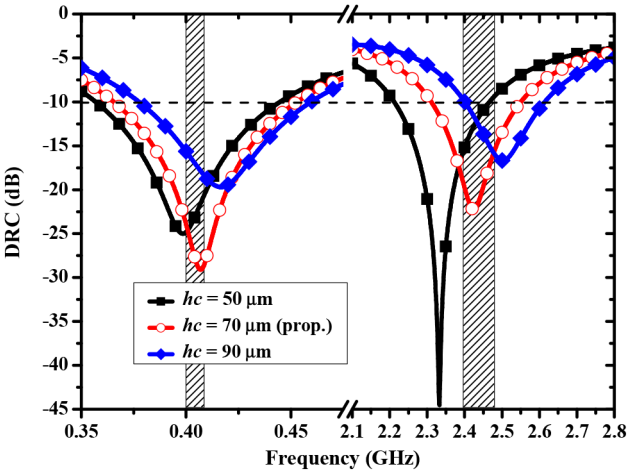

Fig. 15 *Simulated DRCs* (Γ_{dif}) *DRCs for different values of the biocompatible film thickness hc*

fluctuation of <3 dBi between the MICS and ISM bands, mainly because the mismatch at the ISM band caused by the surrounding human tissues is more serious than that at the MICS band and radiation patter at the upper band is less intense in the off-body direction than that at the lower band.

It has to be stressed that for the proposed implantable antenna, health safety regulations have to be considered. As a proof-of-concept demonstration, 10-g average SAR distributions at MICS and ISM bands are computed by setting the differential input power to 1 W for the arm-implanted configuration. Fig. 19 plots the

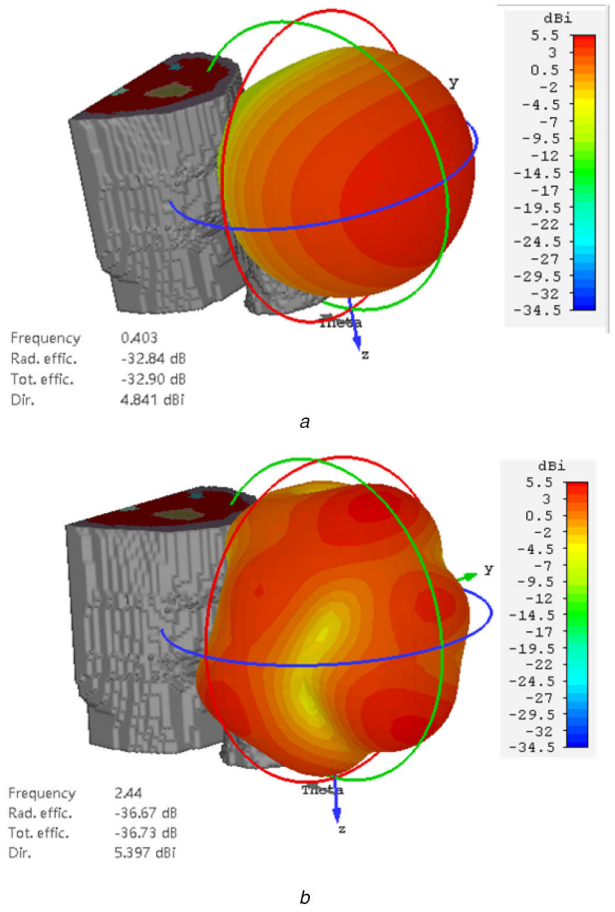

Fig. 16 *3D radiation patterns of the proposed antenna for the arm-implanted configuration*
(a) 403 MHz, ***(b)*** 2.44 GHz

distributions of 10-g average SAR, demonstrating maximum values of 47.9 and 45.5 W/kg at MICS and ISM bands, respectively. However, according to IEEE C95.1–2005 standards [35], the average SAR in a volume of 10-g tissue must be <2 W/kg. As a consequence, the differential input power should not exceed 41.8 mW. Moreover, the ITU-R recommendation specifies the maximum allowable limit of equivalent isotropically radiated power (EIRP) at MICS band to be −16 dBm [36].

EIRP is defined according to the following equation:

$$\text{EIRP} = P_{\text{in}} + G, \tag{9}$$

where P_{in} is the input power in dB and G is the radiation gain of the antenna in dBi. Through (9), to meet the requirement of EIRP, the maximum input power should be <12.1 dBm (16.2 mW). Due to the fact that both SAR and gain values at ISM band are lower than those at MICS band, safety conditions will be satisfied at ISM band if they are met at MICS band. Thus, a differential input power level <16.2 mW would satisfy SAR and EIRP standards for both bands.

3.4 Performance comparison to other implantable antennas

Table 4 summarises the comparison of previously published implantable antennas with the proposed antenna topology.

The tradeoff between radiation gain and volume has been thoroughly investigated. The proposed antenna features the smallest reported volume of 56.45 mm^3. Moreover, the data transfer bandwidth in MICS is larger than most other antennas, whereas pulse-controlling bandwidth in ISM is about 13.1% (2.37–2.69 GHz). It has to be stressed that the proposed antenna features the first-ever reported common-mode rejection ratio K_{CMR}, a unique advantage over all other listed antennas for practical implantable 'noisy' configurations. Compared with [34] that also

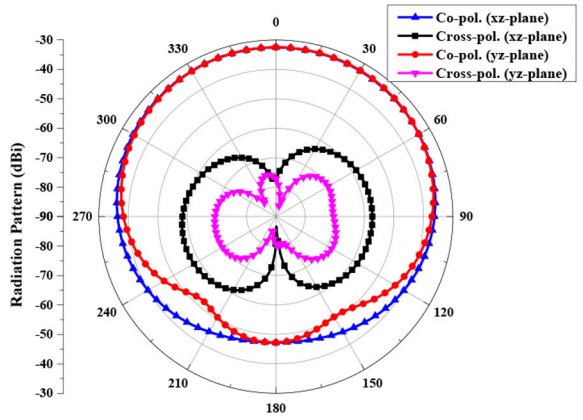

a

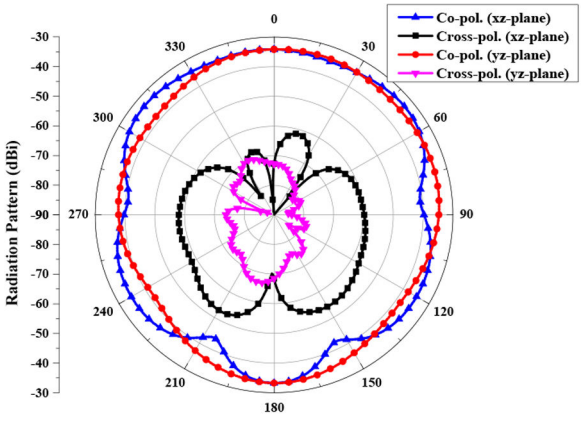

b

Fig. 17 *2D radiation patterns of the proposed antenna in the phantom* ***(a)*** @ 403 MHz, ***(b)*** @ 2.45 GHz

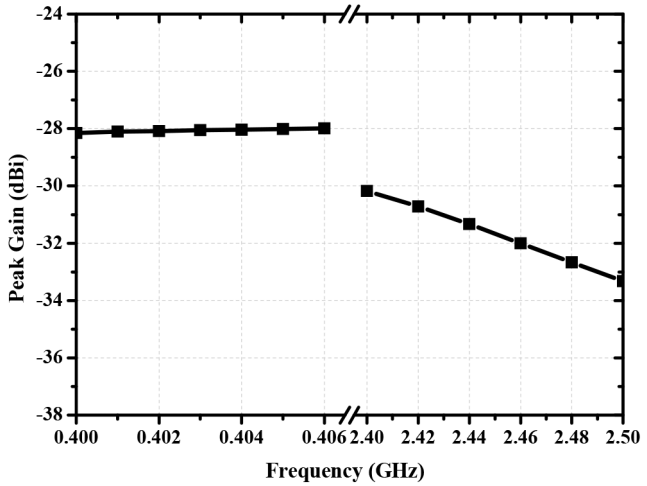

Fig. 18 *Peak gain of the proposed antenna across MICS and 2.44-GHz ISM bands*

employed a differentially fed topology, the proposed antenna has a lower 10-g average SAR, thus being safer for human health.

4 Coating film and in-vitro measurements

To further verify its performance under realistic implantable conditions, the designed antenna was fabricated, and ex-vitro measurements were performed for the antenna prototype shown in Fig. 20*a*. In this work, a thin layer of Al_2O_3 was coated utilising vacuum magnetron sputtering with an aluminium target [37], as shown in Fig. 20*b*.

The film-coating equipment is shown in Fig. 21. Firstly, acetone fluid is used to clean the fabricated antenna, thus enhancing the

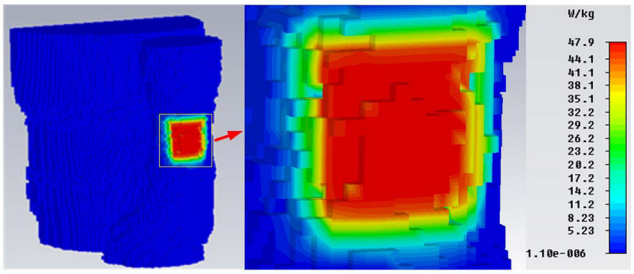

a

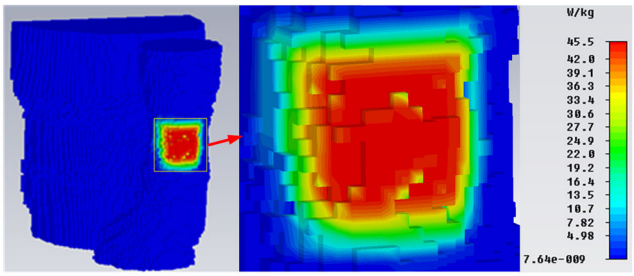

b

Fig. 19 *10-g average SAR distributions for the arm-implanted configuration*
(a) 403 MHz, ***(b)*** 2.44 GHz

Table 4 Comparison of the proposed antenna with other designs

Ref.	Volume, mm^3	Relative bandwidth, %	Peak gain, dBi	K_{CMR}, dB	10-g Avg. SAR (W/kg) (Input power = 1 W)
[24]	1322.5	MICS: 6.79	−26	—	—
		ISM: 7.53	−10	—	—
[9]	594.5	MICS: 2.3	−28.8	—	—
		ISM: 6	−18.5	—	—
[34]	179.0	MICS: 16.5	−30.6	—	63.1
		ISM: 24.7	−19.1	—	76.0
[8]	67.8	MICS: 47.5	−30.5	—	40.3
		ISM: 31.6	−19.2	—	39.2
Prop.	56.45	MICS: 22.8	−28.1	21.24	47.9
		ISM: 13.1	−31.3	2.06	45.5

adhesion of the thin film onto the surface. Then, the antenna is inserted into chamber 1. After closing the flap in chamber 1, vacuum pumps, such as 'roots' and 'molecular' pumps, run in turn to generate a high vacuum environment. Subsequently, the valve between chamber 1 and chamber 2 is opened, then it is closed after the antenna is transferred to the designated position in chamber 2. The film-coating process taking place in chamber 2, is briefly illustrated in Fig. 22. In the beginning, a mixture of the inert gas of argon and oxygen gas is simultaneously pumped into chamber 2. Argon is ionised under high electric voltage and collides with the aluminium target, releasing aluminium atoms. The oxygen gas oxidises the aluminium atoms, depositing a film of alumina on the surface of antenna. During the sputtering, the voltage of power supply is 398 V, the current is 26.1 A, and the air pressure in chamber 2 is 0.93 Pa. Considering the compactness and the adhesion requirements, the deposited film should not be too thick. After 10-hour coating, a film of thickness around 70 μm can be deposited. The coated antenna prototype is shown in Fig. 20*b*.

Owing to its similarity to human tissues, a piece of pork belly, consisting of layers of skin, fat, and muscle, is introduced to function as a human phantom during ex-vitro tests. As shown in Fig. 23, the DRC of the proposed antenna prototype was measured by using a two-port vector network analyser Agilent N5230A when

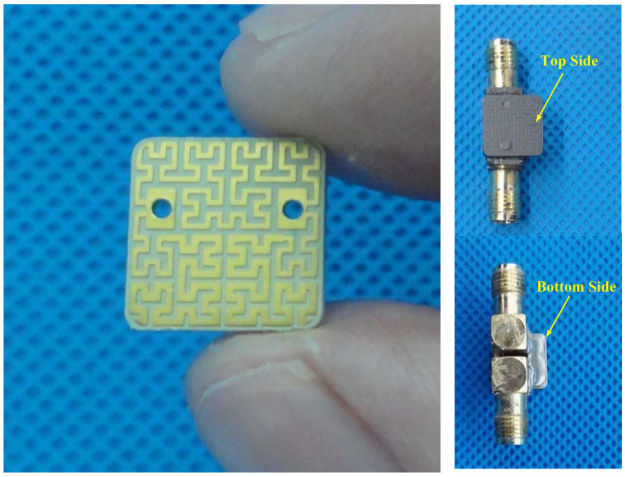

a b

Fig. 20 *Antenna prototype*
(a) Before coating, ***(b)*** After coating

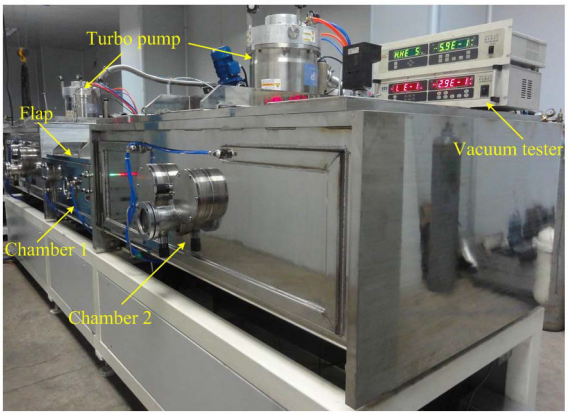

Fig. 21 *Coating machine for the proposed antenna*

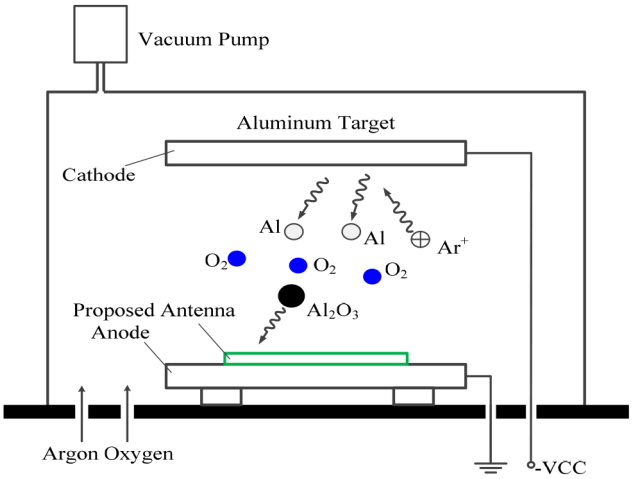

Fig. 22 *Schematic principle of magnetron sputtering*

the antenna implanted into the pork at a depth of $dp3 = 10$ mm. The ex-vitro measured results are illustrated and compared with the simulated results in Fig. 24. With reference to the figure, the measured bandwidths are 92 MHz (359–451 MHz) and 320 MHz (2.37–2.69 GHz) with DRC less than −10 dB at MICS and ISM bands, respectively, indicating a good correlation, especially in the MICS band. Although there is a slight disagreement in the ISM band, the measured curve still covers the whole 2.44-GHz ISM band. This is mainly due to the higher sensitivity of the performance to fabrication tolerances (e.g. SMA connector and soldering) at higher frequencies, as well as to the fact that the

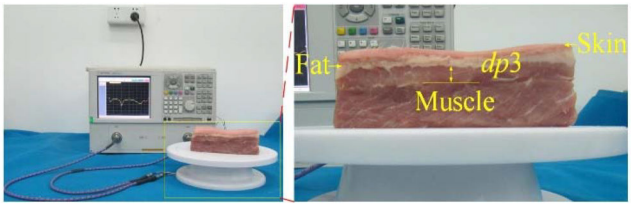

Fig. 23 *Ex-vitro measurement setup for the proposed antenna*

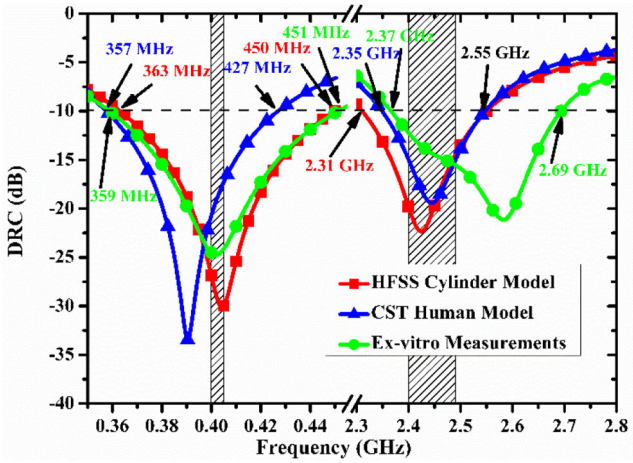

Fig. 24 *Comparison of the measured with the simulated results*

electric properties of the pork belly are slightly different with those utilised in the simulation phantoms.

On account of the significantly lower gain of the implanted antenna and the limited input power of the measurement setup, the far-field EM signal radiated from the antenna under test in a traditional anechoic chamber is easily clogged by the channel noise. In real application, the transmitted signals would be delivered to a long-distance through technological use of signal processing and ways of modulation. Therefore, to make a deep look into the potential communication range and practicability, the relationship between the communication range and the link budget is investigated in the following part.

5 Communication link analysis

To evaluate the wireless communication performance between the implanted antenna and base-station outside the body, the half-wavelength dipole with a realised gain of 2.15 dBi is adopted to work as the external receiver for proof-of-concept demonstration purpose and the losses caused by impedance and polarisation mismatches are neglected. Firstly, the link budget is calculated to analyse far-field communication quality. According to [38], the link margin LM is given by

$$\begin{aligned} M &= \text{Link}\frac{C}{N_0} - \text{Required}\frac{C}{N_0} \\ &= P_t + G_t - L_f + G_r - N_0 - \frac{E_b}{N_0} \\ &\quad - 10\log_{10}B_r + G_c - G_d, \end{aligned} \tag{10}$$

where

$$L_f = 20\log_{10}\left(\frac{4\pi d}{\lambda}\right), \tag{11}$$

and d is the distance between the transmitter and the receiver. The parameters relating to the communication channel used as the basis for the link budget estimation are listed in Table 5.

The computed link margins of the proposed antenna at MICS and ISM bands are shown in Fig. 25. It can be seen that the link margins are both greater than 0 dB within a distance of 10 m when the input power levels are −45 dBm and −30 dBm at MICS and

Table 5 Parameters for link budget estimation

Transmission	
operating frequency, GHz	0.403 / 2.44
Tx power P_t, dBm	−45/–30
Tx antenna Gain G_t, dBi	–28.1 / –31.3
Receiver	
Rx antenna Gain G_r, dBi	2.15
ambient temperature T_0, K	293
receiver noise figure NF, dB	3.5
Boltzmann constant k	1.38×10^{-23}
noise power density N_0, dB/Hz	–199.95
Signal quality	
bit rate B_r, kb/s	7.0
bit error rate	1.0×10^{-5}
E_b/N_0 (ideal-BPSK), dB	9.6
coding gain G_c, dB	0
fixing deterioration G_d, dB	2.5

ISM bands, respectively. Accordingly, at the given maximum input power of 12.1 dBm, the communication range would be larger than 10 m.

Since the near-field boundary of an electric small antenna is $\lambda/2\pi$, its corresponding values at 403 MHz and 2.44 GHz are 118 and 19.5 mm, respectively. Then, in practical cases, the receiver may be within the near-field region of the proposed implantable antenna. Thus, it is necessary to analyse the near-field coupling strength between the transmitting antenna inside and the receiving antenna outside the body. The whole system is regarded as a three-port network. Port 1 and Port 2 lie in the transmitting antenna, while Port 3 belongs to the receiving antenna. According to the definitions of the differential-mode incident wave a_{dif} and of the common-mode incident wave a_{com}, the coupling strength CS can be described as

$$CS = \frac{b_3}{a_{\text{dif}}}\bigg|_{a_{\text{com}}=0 \wedge a_3=0} = \frac{1}{\sqrt{2}}(S_{31} - S_{32}). \quad (12)$$

The computed values of CS at MICS and ISM bands as a function of the distance from 30 to 350 mm are plotted in Fig. 26. Since the power dissipation caused by the lossy human tissue increases with frequency, CS at MICS band is higher than that at ISM band.

6 Conclusion

A novel coated differentially fed implantable dual-band antenna has been introduced in this paper. Integration techniques of high-permittivity substrates, fractal technology and PIFA structures are employed to achieve miniaturisation to a volume of 56.45 mm^3. Dual-band operability in 359–451 MHz and 2.37–2.69 GHz is chosen to enhance the channel capacity while prolonging its operation lifespan. Differential feeding is adopted to suppress common signals and enable easy interfacing with ICs. The distributions of electric field with differential feeding and magnetic field with common-mode feeding have been analysed to thoroughly understand the operation principles, various critical design parameters have been identified and the first-ever reported quantitative evaluation of the noise suppression capability is given for reference purposes. The featured 10-g average SAR distributions with a peak value of 47.9 and 45.5 W/kg satisfy the human safety requirements in both bands. Ex-vitro tests demonstrate a good consistency with the simulated results and the

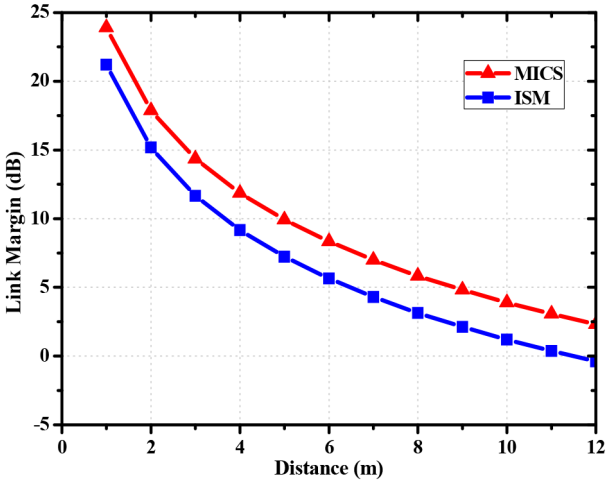

Fig. 25 *Computed link margins of the proposed antenna in far-field communications*

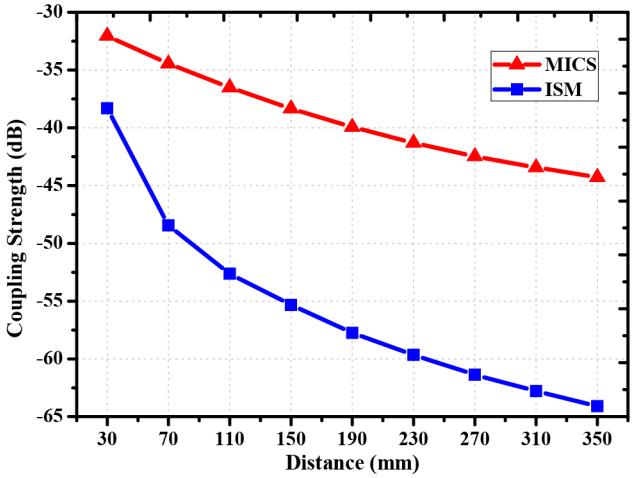

Fig. 26 *Coupling strength between the proposed antenna and the external receiver in near field*

far-field and near-field link budgets of the proposed antenna demonstrate its potential applicability to numerous implantable electronics and biomonitoring applications.

7 References

[1] Hall, P.S., Hao, Y.: '*Antennas and propagation for body-centric wireless communications*' (Artech House, USA, 2012, 2nd Edn.)

[2] Gosalia, P., Lazzi, G., Humayun, M.: 'Investigation of a microwave data telemetry link for a retinal prosthesis', *IEEE Trans. Microw. Theory Tech.*, 2004, **52**, (8), pp. 1925–1933

[3] Valdastri, P., Menciassi, A., Arena, A., *et al.*: 'An implantable telemetry platform system for in vivo monitoring of physiological parameters', *IEEE Trans. Inf. Technol. Biomed.*, 2004, **8**, (3), pp. 271–278

[4] Duan, Z., Guo, Y.X., Xue, R.F., *et al.*: 'Differentially fed dual-band implantable antenna for biomedical applications', *IEEE Trans. Antennas Propag.*, 2012, **60**, (12), pp. 5587–5595

[5] Kiourti, A., Nikita, K.S.: 'Implantable antennas: a tutorial on design, fabrication, and in vitro/in vivo testing', *IEEE Microw. Mag.*, 2014, **15**, (4), pp. 77–91

[6] Kim, J., Rahmat-Samii, Y.: 'Implanted antennas inside a human body: simulations, designs, and characterizations', *IEEE Trans. Microw. Theory Tech.*, 2004, **52**, (8), pp. 1934–1943

[7] Soontornpipt, P., Furse, C.M., Chung, Y.C.: 'Design of implantable microstrip antenna for communication with medical implant', *IEEE Trans. Microw. Theory Tech.*, 2004, **52**, (8), pp. 1944–1951

[8] Xu, L.J., Guo, Y.X., Wu, W.: 'Miniaturized dual-band antenna for implantable wireless communications', *IEEE Antennas Wirel. Propag. Lett.*, 2014, **13**, pp. 1160–1163

[9] Merli, F., Bolomey, L., Zurcher, J.F., *et al.*: 'Design, realization and measurements of a miniature antenna for implantable wireless communication systems', *IEEE Trans. Antennas Propag.*, 2011, **59**, (10), pp. 3544–3555

[10] Liu, C.R., Guo, Y.X., Xiao, S.Q.: 'Capacitively loaded circularly polarized implantable patch antenna for ISM band biomedical applications', *IEEE Trans. Antennas Propag.*, 2014, **62**, (5), pp. 2407–2417

[11] Alrawashdeh, R., Huang, Y., Cao, P.: 'Flexible meandered loop antenna for implants in medradio and ISM bands', *Electron. Lett.*, 2013, **49**, (24), pp. 1515–1517
[12] Li, H., Guo, Y.X., Liu, C.R., *et al.*: 'A miniature-implantable antenna for medradio-band biomedical telemetry', *IEEE Antennas Wirel. Propag. Lett.*, 2015, **14**, pp. 1176–1179
[13] Liu, X.Y., Wu, Z.T., Fan, Y., *et al.*: 'A miniaturized CSRR loaded wide-beamwidth circularly polarized implantable antenna for subcutaneous real-time glucose monitoring', *IEEE Antennas Wirel. Propag. Lett.*, 2017, **16**, pp. 577–580
[14] Kiourti, A., Nikita, K.S.: 'Miniature scalp-implantable antennas for telemetry in the MICS and ISM bands: design, safety considerations and link budget analysis', *IEEE Trans. Antennas Propag.*, 2012, **60**, (8), pp. 3568–3575
[15] Goswami, C., Ghatak, R., Poddar, D.R.: 'Multi-band bisected Hilbert monopole antenna loaded with multiple subwavelength split-ring resonators', *IET Microw., Antennas Propag.*, 2018, **12**, (10), pp. 1719–1727
[16] Wang, Y.Q, Wang, Z., Li, J.F.: 'UHF Moore fractal antennas for online GIS PD detection', *IEEE Antennas Wirel. Propag. Lett.*, 2017, **16**, pp. 852–855
[17] Taghadosi, M., Albasha, L., Qaddoumi, N., *et al.*: 'Miniaturised printed elliptical nested fractal multiband antenna for energy harvesting applications', *IET Microw., Antennas Propag.*, 2015, **9**, (10), pp. 1045–1053
[18] Chen, Z.N., Liu, G.C., See, T.S.P.: 'Transmission of RF signals between MICS loop antennas in free space and implanted in the human head', *IEEE Trans. Antennas Propag.*, 2009, **57**, (6), pp. 1850–1854
[19] Li, R.Q., Xiao, S.Q.: 'Compact slotted semi-circular antenna for implantable medical devices', *Electron. Lett.*, 2014, **50**, (23), pp. 1675–1677
[20] Yang, C.L., Tsai, C.L., Chen, S.H.: 'Implantable high-gain dental antennas for minimally invasive biomedical devices', *IEEE Trans. Antennas Propag.*, 2013, **61**, (5), pp. 2380–2387
[21] Bradley, P.D.: 'An ultra low power, high performance medical implant communication system (MICS) transceiver for implantable devices'. Proc. IEEE Biomed. Circuits and Syst. Conf. (BioCAS), London, UK, November 2006, pp. 158–161
[22] Liu, H., Liu, X.Y.: 'A miniaturized differentially fed implantable Hilbert curve fractal antenna at MICS band'. Proc. 1st IEEE Int. Conf. on Computational Electromagnetics (ICCEM), Hong Kong, China, February 2015, pp. 275–277
[23] Abadia, J., Merli, F., Zurcher, J.F., *et al.*: '3D spiral small antenna design and realization for biomedical telemetry in the MICS band', *Radioengineering*, 2009, **18**, (4), pp. 359–367
[24] Karacolak, T., Cooper, R., Topsakal, E.: 'Electrical properties of rat skin and design of implantable antennas for medical wireless telemetry', *IEEE Trans. Antennas Propag.*, 2009, **57**, (9), pp. 2806–2812
[25] Xu, L.J., Guo, Y.X., Wu, W.: 'Miniaturized circularly polarized loop antenna for biomedical applications', *IEEE Trans. Antennas Propag.*, 2015, **63**, (3), pp. 922–930
[26] Medical Implantable RF Transceiver ZL70102 Data Sheet, Zarlink Semiconductor, Ottawa, ON, Canada, October 2006
[27] Bockelman, D.E., Eisenstadt, W.R.: 'Combined differential and common-mode scattering parameters: theory and simulation', *IEEE Trans. Microw. Theory Tech.*, 1995, **43**, (7), pp. 1530–1539
[28] Gabriel, S., Lau, R.W., Gabriel, C.: 'The dielectric properties of biological tissues: III. Parametric models for the dielectric spectrum of tissues', *Phys. Med. Biol.*, 1996, **41**, (11), pp. 2271–2293
[29] Wang, F., Bin, F., Sun, Q.Q., *et al.*: 'A compact UHF antenna based on complementary fractal technique', *IEEE. Access.*, 2017, **5**, pp. 21118–21125
[30] Arif, A., Zubair, M., Ali, M., *et al.*: 'A compact, low-profile fractal antenna for wearable on-body WBAN applications', *IEEE Antennas Wirel. Propag. Lett.*, 2019, **18**, (5), pp. 981–985
[31] Mondal, T., Maity, S., Ghatak, R., *et al.*: 'Compact circularly polarized wide-beamwidth fern-fractal-shaped microstrip antenna for vehicular communication', *IEEE Trans. Veh. Technol.*, 2018, **67**, (6), pp. 5126–5134
[32] Zubal, I.G., Harrell, C.R., Smith, E.O., *et al.*: 'Computerized three-dimensional segmented human anatomy', *Med. Phys.*, 1994, **21**, (2), pp. 299–302
[33] 'The Zubal Phantom data, Arms down phantom data description', http://noodle.med.yale.edu/phantom/ getdw-ndesc.htm, accessed 4 October 2018
[34] Duan, Z., Guo, Y.X., Je, M., *et al.*: 'Design and in *vitro* test of a differentially fed dual-band implantable antenna operating at MICS and ISM bands', *IEEE Trans. Antennas Propag.*, 2014, **62**, (5), pp. 2430–2439
[35] IEEE Standard C95.1–2005.: 'IEEE standard for safety levels with respect to human exposure to radiofrequency electromagnetic fields, 3 kHz to 300 GHz', 2006
[36] Rec. ITU-R SA.1346, Int. Telecommun. Union, Geneva, Switzerland, 1998
[37] 'Sputter deposition', https://en.wikipedia.org/wiki/Sputt-er_deposition, accessed 4 October 2018
[38] Wei, X., Saito, K., Takahashi, M., *et al.*: 'Performances of an implanted cavity slot antenna embedded in the human arm', *IEEE Trans. Antennas Propag.*, 2009, **57**, (4), pp. 894–899